The Journal of Chemical Physics

Electron transfer in photoexcited pyrrole dimers

Cite as: J. Chem. Phys. **151**, 164304 (2019); https://doi.org/10.1063/1.5120006
Submitted: 17 July 2019 . Accepted: 01 October 2019 . Published Online: 25 October 2019

Simon P. Neville, Adam Mirmiran, Graham A. Worth, and Michael S. Schuurman

View Online Export Citation CrossMark

ARTICLES YOU MAY BE INTERESTED IN

Adventures in DFT by a wavefunction theorist
The Journal of Chemical Physics **151**, 160901 (2019); https://doi.org/10.1063/1.5116338

Accurate and efficient DFT-based diabatization for hole and electron transfer using absolutely localized molecular orbitals
The Journal of Chemical Physics **151**, 164114 (2019); https://doi.org/10.1063/1.5125275

Exact and approximate symmetry projectors for the electronic structure problem on a quantum computer
The Journal of Chemical Physics **151**, 164111 (2019); https://doi.org/10.1063/1.5110682

Challenge us.
What are your needs for periodic signal detection?
Zurich Instruments
Watch

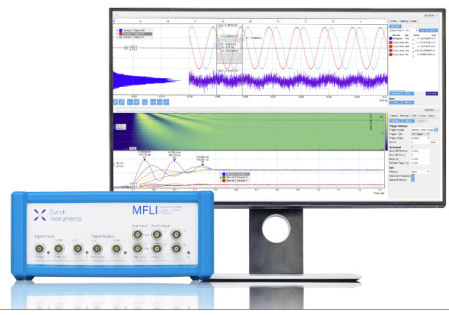

AIP Publishing

© 2019 Author(s).

The Journal of Chemical Physics ARTICLE scitation.org/journal/jcp

Electron transfer in photoexcited pyrrole dimers

Cite as: J. Chem. Phys. 151, 164304 (2019); doi: 10.1063/1.5120006
Submitted: 17 July 2019 • Accepted: 1 October 2019 •
Published Online: 24 October 2019

View Online Export Citation CrossMark

Simon P. Neville,[1,a)] Adam Mirmiran,[2,b)] Graham A. Worth,[3] and Michael S. Schuurman[1,2,c)]

AFFILIATIONS

[1] Department of Chemistry and Biomolecular Sciences, University of Ottawa, 10 Marie Curie, Ottawa, Ontario K1N 6N5, Canada
[2] National Research Council of Canada, 100 Sussex Drive, Ottawa, Ontario K1A 0R6, Canada
[3] Department of Chemistry, University College London, 20 Gordon Street, London WC1H 0AJ, United Kingdom

[a)] **Current address:** National Research Council of Canada, 100 Sussex Drive, Ottawa, Ontario K1A 0R6, Canada.
[b)] **Current address:** Department of Chemistry and Biomolecular Sciences, University of Ottawa, 10 Marie Curie, Ottawa, Ontario K1N 6N5, Canada.
[c)] **Electronic mail:** michael.schuurman@nrc-cnrc.gc.ca

ABSTRACT

Following on from previous experimental and theoretical work [Neville *et al.*, Nat. Commun. 7, 11357 (2016)], we report the results of a combined electronic structure theory and quantum dynamics study of the excited state dynamics of the pyrrole dimer following excitation to its first two excited states. Employing an exciton-based analysis of the $\tilde{A}(\pi 3s/\sigma^*)$ and $\tilde{B}(\pi 3s/3p/\sigma^*)$ states, we identify an excited-state electron transfer pathway involving the coupling of the $\tilde{A}(\pi 3s/\sigma^*)$ and $\tilde{B}(\pi 3s/3p/\sigma^*)$ states and driven by N–H dissociation in the $\tilde{B}(\pi 3s/3p/\sigma^*)$ state. This electron transfer mechanism is found to be mediated by vibronic coupling of the $\tilde{B}$ state, which has a mixed $\pi 3s/3p$ Rydberg character at the Franck-Condon point, to a high-lying charge transfer state of the $\pi\sigma^*$ character by the N–H stretch coordinate. Motivated by these results, quantum dynamics simulations of the excited-state dynamics of the pyrrole dimer are performed using the multiconfigurational time-dependent Hartree method and a newly developed model Hamiltonian. It is predicted that the newly identified electron transfer pathway will be open following excitation to both the $\tilde{A}(\pi 3s/\sigma^*)$ and $\tilde{B}(\pi 3s/3p/\sigma^*)$ states and may be the dominant relaxation pathway in the latter case.

Published under license by AIP Publishing. https://doi.org/10.1063/1.5120006

I. INTRODUCTION

The photochemistry and photophysics of isolated heteroaromatic molecules have been the subject of many experimental and theoretical studies.[1–18] This interest has been driven in part because molecules in this class are considered as useful, tractable models for the DNA nucleobases and, by extension, nucleotides. The excited-state dynamics initiated by electronic excitation in a large number of heteroaromatic molecules is now well understood. Particular attention has been paid to the role of low-lying singlet states of the $\pi 3s$ character which, via coupling to higher-lying $\pi\sigma^*$ states, are quasibound with respect to X–H stretching (where X denotes a heteroatom). When populated, dissociation in these $\pi 3s/\sigma^*$ states is known to provide a universal electronic relaxation mechanism in heteroaromatic molecules.[2]

While isolated heteroaromatic molecules have proved to be experimentally useful and computationally tractable models for mononucleotides, their use in the understanding of the photoinduced dynamics of polynucleotides is somewhat limited. This is because the interactions of the individual nucleobases in a polynucleotide can lead to additional de-excitation pathways that are absent in the mononucleotide case, including excited-state charge transfer[19,20] and proton-coupled electron transfer.[21] Additionally, delocalization of the excited electronic states over multiple nucleotides is believed to occur at near-Franck-Condon (FC) point geometries in polynucleotides.[22–24] Clearly, the understanding of these processes cannot be enhanced via the study of isolated heteroaromatic molecules.

As a first step on the ladder to understand the role of charge transfer in polynucleotides, one may turn to dimers of heteroaromatic molecules. These systems are small enough to afford a detailed, high-level theoretical treatment, while also being able to support the types of electronic states known to be important in photoexcited polynucleotides, that is, both charge transfer states and delocalized FC region states. Unlike the heteroaromatic monomers, however, the excited-state dynamics of heteroaromatic dimers has been much less studied.

Published under license by AIP Publishing

A notable exception here is the pyrrole dimer, for which a low-lying charge transfer (CT) state has been speculated to be populated following photoexcitation.[25,26] In particular, in Ref. 25, a combination of time-resolved photoelectron spectroscopy (TRPES) and static electronic structure calculations was used to infer the participation of a low-lying state of CT character following excitation of the pyrrole dimer with photon wavelengths of 245 and 240 nm. Although the initial measurements were not cluster size-selected, this interpretation was subsequently verified in the size-selected time-resolved ion imaging study of Montero *et al.*[26]

While the photochemistry of the pyrrole dimer has been explored to some extent using static electronic structure calculations,[25,27] to date, there does not exist any extensive simulations of its excited state dynamics. We here seek to remedy this via the use of fully quantum dynamical calculations of the pyrrole dimer following excitation to its first two excited states. To do so, a new model Hamiltonian is constructed to describe the vibronically coupled dynamics in this electronic state manifold and used in multiconfigurational time-dependent Hartree (MCTDH) simulations.

We predict that the first two excited states of the pyrrole dimer are delocalized at the FC point. However, due to nuclear dynamics involving N–H stretching, the second excited state develops a charge transfer character on a sub-100 fs time scale following vertical excitation to it. Importantly, this appears to be somewhat analogous in nature to the nuclear dynamics-driven charge transfer recently observed in model dinucleotides[28] and suggests that heteroaromatic dimers may provide fruitful grounds for an understanding of the mechanisms underlying charge transfer in polynucleotide systems.

II. METHODOLOGY

In the following, we adopt a quasidiabatic representation of the molecular Hamiltonian. We consider two electronic states: $\tilde{A}(\pi 3s/\sigma^*)$ and $\tilde{B}(\pi 3s/3p/\sigma^*)$. At the FC point, these states correlate with the S_1 and S_2 states and are of A'' symmetry. The somewhat cumbersome labeling used here is meant to reflect the changes in the characters of the quasidiabatic states with nuclear geometry. As discussed in detail in Sec. III B, the $\tilde{A}$ state has a $\pi 3s$ Rydberg character at the FC point but develops a valence $\pi\sigma^*$ character as one of the N–H bonds is broken. Similarly, the $\tilde{B}$ state has a mixed $\pi 3s/\pi 3p$ character at the FC point but acquires a $\pi\sigma^*$ character as the N–H bond is stretched. This is analogous to the change in the character of the $A_2(\pi 3s)$ and $B_1(\pi 3s)$ states of the monomer upon N–H dissociation.

We are particularly interested in the possibility of CT occurring following excitation to the $\tilde{A}(\pi 3s/\sigma^*)/\tilde{B}(\pi 3s/3p/\sigma^*)$ state manifold. In Sec. II D, we describe our methodology for determining the CT characters of these states as a function of nuclear geometry. In Sec. II B, we describe the details of our quantum dynamics simulations that are used in conjunction with this analysis to determine the likelihood of CT occurring following excitation to the $\tilde{A}(\pi 3s/\sigma^*)$ and $\tilde{B}(\pi 3s/3p/\sigma^*)$ states.

A. Labeling conventions

For reference, we show in Fig. 1 the ground state minimum energy geometry of the pyrrole dimer. Here and throughout, we label the monomer with the free N–H bond pointing into the vacuum as monomer *a* and the monomer whose N–H bond is directed toward the π-system of monomer *a* as monomer *b*.

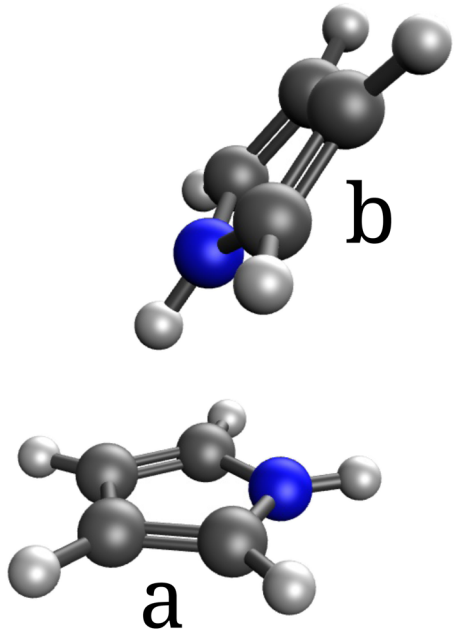

FIG. 1. Ground state minimum energy geometry of the pyrrole dimer calculated at the SCS-MP2/aug-cc-pVDZ level of theory. Here and throughout, the monomer with the free N–H bond pointing into the vacuum is labeled *a* and the other monomer is labeled *b*.

B. The model Hamiltonian

We represent the Hamiltonian in a two-state quasidiabatic basis spanned by the $\tilde{A}(\pi 3s/\sigma^*)$ and $\tilde{B}(\pi 3s/3p/\sigma^*)$ states,

$$\boldsymbol{H} = \hat{T}_n \begin{bmatrix} 1 & 0 \\ 0 & 1 \end{bmatrix} + \begin{bmatrix} W_{11} & W_{12} \\ W_{21} & W_{22} \end{bmatrix}. \quad (1)$$

Here, $\hat{T}_n$ denotes the nuclear kinetic energy operator. W_{11} and W_{22} are the diabatic potential energy surfaces for the $\tilde{A}$ and $\tilde{B}$ states, respectively, and W_{12} describes the vibronic coupling between these two states.

1. Choice of nuclear coordinates and the kinetic energy operator

To proceed, a set of nuclear coordinates suitable for the description of the excited-state dynamics of the pyrrole dimer must be chosen. Our previous work highlighted two coordinates for which large amplitude motion could be expected to occur along following electronic excitation to the $\tilde{A}/\tilde{B}$ state manifold.[25] These were (i) r, the length of the N–H bond of monomer *a*, and (ii) R, the length of the vector connecting the centers of mass of the two monomers. For reference, the adiabatic potentials calculated at the DFT/MRCI/aug-cc-pVDZ level of theory along these coordinates are shown in Fig. 2.

Published under license by AIP Publishing

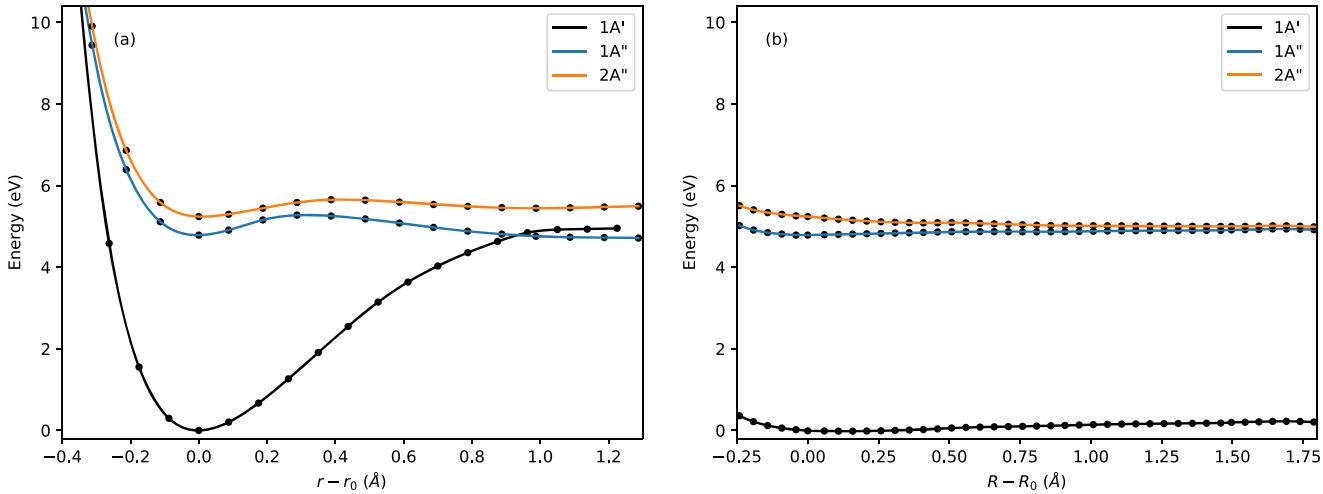

FIG. 2. Adiabatic potential energy surfaces calculated at the DFT/MRCI/aug-cc-pVDZ level of theory for the 1*A*′, 1*A*″, and 2*A*″ states along: (a) the monomer *a* N–H stretching coordinate, *r*, and (b) the monomerization coordinate *R*.

Guided by this, we chose the first two of the $3N$ nuclear coordinates of our model to be the lengths of mass-weighted vectors corresponding to r and R, denoted by $\tilde{r}$ and $\tilde{R}$. The remaining $3N-2$ coordinates were chosen to be derived from the set $\{\tilde{q}_\alpha\}$ of eigenvectors of the mass-weighted ground state Hessian after projection onto the space orthogonal to the coordinates $\tilde{r}$ and $\tilde{R}$. The procedure for the construction of these "projected normal modes" is detailed in Appendix A.

The set of coordinates $\{\tilde{r}, \tilde{R}, \tilde{q}_\alpha : \alpha = 1, \ldots, 3N-2\}$ is derived from an orthogonal transformation of the mass-scaled Cartesian coordinates $\tilde{x}_i$. As such, the nuclear kinetic energy operator adopts a diagonal form in this coordinate system,

$$\hat{T}_n = -\frac{1}{2}\left(\frac{\partial^2}{\partial \tilde{r}^2} + \frac{\partial^2}{\partial \tilde{R}^2} + \sum_{\alpha=1}^{3N-2} \frac{\partial^2}{\partial \tilde{q}_\alpha^2}\right). \tag{2}$$

Finally, in order to make the grids used in the quantum dynamics calculations more uniform, we make the replacements

$$\tilde{q}_\alpha \to \tilde{Q}_\alpha = \sqrt{\mathcal{W}_\alpha}\tilde{q}_\alpha, \tag{3}$$

$$\tilde{r} \to \bar{r} = \sqrt{\mathcal{W}_{\tilde{r}}}\tilde{r}, \tag{4}$$

$$\tilde{R} \to \bar{R} = \sqrt{\mathcal{W}_{\tilde{R}}}\tilde{R}, \tag{5}$$

where $\mathcal{W}_\alpha = \sqrt{\frac{\partial^2 V_0}{\partial \tilde{q}_\alpha^2}}$ is evaluated at the FC point, and $\mathcal{W}_{\tilde{r}}$ and $\mathcal{W}_{\tilde{R}}$ are defined analogously. It is the coordinate set $\{\bar{r}, \bar{R}, \bar{Q}_\alpha : \alpha = 1, \ldots, 3N-2\}$ that we used in our quantum dynamics simulations. The form of the nuclear kinetic energy operator in this coordinate system reads

$$\hat{T}_n = -\frac{1}{2}\left(\mathcal{W}_{\tilde{r}}\frac{\partial^2}{\partial \bar{r}^2} + \mathcal{W}_{\tilde{R}}\frac{\partial^2}{\partial \bar{R}^2} + \sum_{\alpha=1}^{3N-2} \mathcal{W}_\alpha \frac{\partial^2}{\partial \bar{Q}_\alpha^2}\right). \tag{6}$$

2. The model diabatic potential

Our 2 × 2 model quasidiabatic potential matrix, $\boldsymbol{W}(\bar{r}, \bar{R}, \bar{\boldsymbol{Q}})$, takes the form of a sum of uncorrelated subsystem potentials plus an interaction potential coupling the dissociative degree of freedom $\bar{r}$ to the bound projected normal modes $\bar{Q}_\alpha$,

$$\boldsymbol{W}(\bar{r}, \bar{R}, \bar{\boldsymbol{Q}}) = \boldsymbol{W}(\bar{r}) + \boldsymbol{W}(\bar{R}) + \boldsymbol{W}(\bar{\boldsymbol{Q}}) + \boldsymbol{W}^{(int)}(\bar{r}, \bar{\boldsymbol{Q}}). \tag{7}$$

Briefly, the subsystem potential $\boldsymbol{W}(\bar{\boldsymbol{Q}})$ for the bound degrees of freedom $\bar{Q}_\alpha$ is taken as a truncated second-order vibronic coupling Hamiltonian.[29,30] The uncorrelated contributions from the unbound coordinates $\bar{r}$ and $\bar{R}$ were taken as functions exhibiting the correct asymptotic behaviors. The on-diagonal elements of the quasidiabatic potential with respect to these two degrees of freedom were modeled as avoided-crossing potentials, while the coupling between the $\tilde{A}$ and $\tilde{B}$ states was taken to assume a hyperbolic tangent form. The correlation between the bound degrees of freedom $\bar{Q}_\alpha$ and the dissociative N–H dissociation coordinate $\bar{r}$ was dealt with through the use of switching functions. The full details of the form of the model potential are given in Appendix B.

The parameters of the model potential were determined by fitting to adiabatic energies calculated at a large number of nuclear geometries along individual degrees of freedom and combinations of projected normal modes $\bar{Q}_\alpha$ and the N–H dissociation coordinate $\bar{r}$. For this, adiabatic energies were calculated at the DFT/MRCI/aug-cc-pVDZ level of theory. All other details of the fitting procedure are given in Appendix C.

C. Wavepacket propagation calculations

Wavepacket propagations were performed using the multiconfigurational time-dependent Hartee (MCTDH) method,[31–33] as

Published under license by AIP Publishing

implemented in the Quantics quantum dynamics package.[34] The details of these calculations, along with a discussion of the calculation of N–H dissociation probabilities, are given in Appendixes D and E.

D. Charge transfer analysis

We require a means of determining the CT character of the $\tilde{A}(\pi 3s/\sigma^*)$ and $\tilde{B}(\pi 3s/3p/\sigma^*)$ states at the geometries sampled by the evolving wavepacket following photoexcitation. To do so, we make use of an exciton-based analysis of the electronic wavefunctions. For the transition from the electronic state $|\Phi_\sigma\rangle$ to the state $|\Phi_{\sigma'}\rangle$, it can be shown that the associated transition density

$$\gamma^{(\sigma,\sigma')}(\boldsymbol{x}_h,\boldsymbol{x}_e) = N\int_{-\infty}^{\infty}\{\Phi_\sigma^*(\boldsymbol{x}_h,\boldsymbol{x}_2,\ldots,\boldsymbol{x}_N) \times\Phi_{\sigma'}(\boldsymbol{x}_e,\boldsymbol{x}_2,\ldots,\boldsymbol{x}_N)d\boldsymbol{x}_2\cdots\boldsymbol{x}_N\} \tag{8}$$

corresponds exactly (up to a sign) to an exciton wavefunction $\chi_{exc}^{(\sigma,\sigma')}(\boldsymbol{x}_h,\boldsymbol{x}_e)$ describing the correlated motion of hole and electron quasiparticles created by the electronic transition.[35–38] Here, $\boldsymbol{x}$ is used to denote the one-particle coordinates.

The exciton wavefunction $\chi_{exc}^{(\sigma,\sigma')}(\boldsymbol{x}_h,\boldsymbol{x}_e)$ can be used to assess the degree of CT involved in the transition between $|\Phi_\sigma\rangle$ and $|\Phi_{\sigma'}\rangle$ in a number of ways. First, the hole and electron densities, defined as

$$\rho_h^{(\sigma,\sigma')}(\boldsymbol{x}_h) = \int_{-\infty}^{\infty}\left|\chi_{exc}^{(\sigma,\sigma')}(\boldsymbol{x}_h,\boldsymbol{x}_e)\right|^2 d\boldsymbol{x}_e \tag{9}$$

and

$$\rho_e^{(\sigma,\sigma')}(\boldsymbol{x}_e) = \int_{-\infty}^{\infty}\left|\chi_{exc}^{(\sigma,\sigma')}(\boldsymbol{x}_h,\boldsymbol{x}_e)\right|^2 d\boldsymbol{x}_h, \tag{10}$$

respectively, may be visualized. The hole (electron) density gives the probability of the hole (electron) being at a location $\boldsymbol{x}$. Thus, if the hole and electron densities are localized on different monomers, then one may draw the conclusion that a high degree of CT has occurred due to the electronic transition in question.

Second, the degree of CT may be quantified by a consideration of the exciton size and hole-electron distances. The exciton size, $d_{exc}^{(\sigma,\sigma')}$, is defined as the root mean square (RMS) separation between the instantaneous hole and electron positions,

$$d_{exc}^{(\sigma,\sigma')} = \sqrt{\left\langle|\boldsymbol{x}_h-\boldsymbol{x}_e|^2\right\rangle_{exc}^{(\sigma,\sigma')}}. \tag{11}$$

Here, the notation $\langle\hat{O}\rangle_{exc}^{(\sigma,\sigma)}$ is used to denote the exciton expectation value of the operator $\hat{O}$,

$$\langle\hat{O}\rangle_{exc}^{(\sigma,\sigma)} = \frac{\left\langle\chi_{exc}^{(\sigma,\sigma')}\middle|\hat{O}\middle|\chi_{exc}^{(\sigma,\sigma')}\right\rangle}{\left\langle\chi_{exc}^{(\sigma,\sigma')}\middle|\chi_{exc}^{(\sigma,\sigma')}\right\rangle}. \tag{12}$$

The hole-electron distance, $d_{h\to e}^{(\sigma,\sigma')}$, is defined as the distance between the centroids of the hole and electron densities,

$$d_{h\to e}^{(\sigma,\sigma')} = \left|\langle\boldsymbol{x}_e\rangle_{exc}^{(\sigma,\sigma')} - \langle\boldsymbol{x}_h\rangle_{exc}^{(\sigma,\sigma')}\right|. \tag{13}$$

For an electronic transition that is of CT character, the corresponding exciton size and the hole-electron distance will both scale as the intermonomer separation. This provides a quantitative measure of the degree of CT character of the transition.

In the case of the pyrrole dimer, we are interested in the CT characters of the quasidiabatic $\tilde{A}(\pi 3s/\sigma^*)$ and $\tilde{B}(\pi 3s/3p/\sigma^*)$ states. We thus calculated the electron and hole densities, exciton sizes, and hole-electron distances for the $\tilde{A}(\pi 3s/\sigma^*) \leftarrow \tilde{X}$ and $\tilde{B}(\pi 3s/3p/\sigma^*) \leftarrow \tilde{X}$ transitions at geometries of interest with respect to the photo-induced dynamics. This requires the calculation of the quasidiabatic electronic states, which are not directly available from electronic structure calculations. To overcome this, the electronic states in the adiabatic representation were first calculated and transformed to the quasidiabatic representation using the eigenvector matrix of the model quasidiabatic potential used in the quantum dynamics simulations (as discussed in Sec. II B). The adiabatic electronic states were calculated at the DFT/MRCI/aug-cc-pVDZ level of theory, which in previous work was found to provide a good level of agreement with experimental observations.[25] In these calculations, the redesigned Hamiltonian of Lyskov *et al.* was used,[39] which is known to give a correct description of dimer states, even in the limit of large intermonomer separations.[40]

III. RESULTS

A. Low-lying excited states of the pyrrole dimer

We begin with a brief discussion of the low-lying singlet excited states of the pyrrole dimer at the FC point. Shown in Table I are the DFT/MRCI/aug-cc-pVDZ vertical excitation energies, oscillator strengths, and dominant natural transition orbitals[41] (NTOs) of the excited states lying below 6 eV. The states spanning this energy interval are predicted to be of either the $\pi\pi^*$ or 3*s* and 3*p* Rydberg character. In addition to the existence of locally excited (LE) states of $\pi\pi^*$ character, many Rydberg states of a delocalized electronic character are also found to lie in this energy range, with either or both the dominant hole/particle NTOs being delocalized across both monomers. Importantly, from the NTO analysis presented here, it does not appear that any low-lying states of CT character exist at the FC point. However, the electronic characters of the first two excited states are found to change significantly as a function of the N–H bond length of monomer *a*, leading to the opening of a CT pathway. This is discussed in detail in Sec. III B.

B. N–H dissociation-driven charge transfer

Here, we discuss the evolution of the electronic characters of the $\tilde{A}(\pi 3s/\sigma^*)$ and $\tilde{B}(\pi 3s/3p/\sigma^*)$ diabatic states as a function of the N–H bond length of the monomer *a*.

At the FC point, the DFT/MRCI/aug-cc-pVDZ vertical excitation energies of the $\tilde{A}(\pi 3s/\sigma^*)$ and $\tilde{B}(\pi 3s/3p/\sigma^*)$ states are 4.79 eV and 5.24 eV, respectively. In Fig. 3, we show the electron and hole densities for the $\tilde{A}(\pi 3s/\sigma^*) \leftarrow \tilde{X}$ and $\tilde{B}(\pi 3s/3p/\sigma^*) \leftarrow \tilde{X}$ transitions at the FC point and at an elongated monomer *a* N–H bond length just within the dissociation limit (4.3 a.u.). At the FC point, the $\tilde{A}(\pi 3s/\sigma^*)$ state hole density is found to correspond to

Published under license by AIP Publishing

TABLE I. Vertical excitation energies (ΔE), oscillator strengths (f), and dominant NTO pairs of the low-lying excited states of the pyrrole dimer as calculated at the DFT/MRCI/aug-cc-pVDZ level of theory. The numbers in parentheses alongside the NTO pairs are corresponding to the weights (squared singular values). The subscripts a and b are used to denote the monomer on which a given NTO is localized. A subscript of ab indicates that the NTO is delocalized across both monomers.

State	ΔE (eV)	f	NTOs
$1A''$	4.79	0.005	$\pi_b \rightarrow 3s_{ab}$ (0.95)
$2A''$	5.24	0.027	$\pi_{ab} \rightarrow 3p_{ab}$ (0.62)
			$\pi_{ab} \rightarrow 3s_{ab}$ (0.34)
$3A''$	5.32	0.017	$\pi_b \rightarrow 3p_{ab}$ (0.60)
			$\pi_a \rightarrow 3s_{ab}$ (0.36)
$2A'$	5.32	0.039	$\pi_b \rightarrow 3p_{ab}$ (0.94)
$4A''$	5.56	0.000	$\pi_b \rightarrow 3p_{ab}$ (0.88)
$5A''$	5.57	0.000	$\pi_b \rightarrow \pi_a^*$ (0.90)
$3A'$	5.60	0.001	$\pi_b \rightarrow \pi_b^*$ (0.56)
			$\pi_b \rightarrow \pi_b^*$ (0.33)
$4A'$	5.74	0.007	$\pi_b \rightarrow 3s_{ab}$ (0.58)
			$\pi_{ab} \rightarrow \pi_a^*$ (0.17)
			$\pi_a \rightarrow \pi_a^*$ (0.12)
$5A'$	5.78	0.001	$\pi_a \rightarrow \pi_a^*$ (0.36)
			$\pi_a \rightarrow \pi_a^*$ (0.28)
			$\pi_b \rightarrow \pi_b^*$ (0.21)
$6A''$	5.89	0.032	$\pi_a \rightarrow 3p_a$ (0.65)
			$\pi_b \rightarrow \pi_{ab}^*$ (0.30)
$6A'$	5.89	0.020	$\pi_a \rightarrow 3p_a$ (0.66)
			$\pi_b \rightarrow 3p_b$ (0.22)
$7A''$	5.92	0.135	$\pi_{ab} \rightarrow \pi_a^*$ (0.64)
			$\pi_{ab} \rightarrow 3d_{ab}$ (0.28)
$8A''$	5.98	0.165	$\pi_b \rightarrow \pi_{ab}^*$ (0.65)
			$\pi_a \rightarrow 3p_a$ (0.26)

excitation from a π-type orbital on monomer b, while the electron density is diffuse and Rydberg-like, being delocalized over the whole dimer. The $\tilde{B}(\pi 3s/3p/\sigma^*)$ state hole density at the FC point corresponds to two π-type orbitals, one localized on each monomer, while the electron density is again Rydberg-like and delocalized over the two monomers. We thus conclude that at the FC point, neither the $\tilde{A}(\pi 3s/\sigma^*)$ nor the $\tilde{B}(\pi 3s/3p/\sigma^*)$ state has the charge transfer character, with the electron density being completely delocalized in both cases and the hole density also being delocalized in the case of the $\tilde{B}(\pi 3s/3p/\sigma^*)$ state. The situation, however, is found to change upon stretching of the N–H bond of monomer a. Analogous to case of the isolated pyrrole monomer, elongation of the N–H bond is found to result in a change in the electronic characters of these two Rydberg-type states due to coupling to higher lying states of the $\pi\sigma^*$ character. This is clearly seen in the dissociation limit electron and hole densities shown in Fig. 3. Importantly, the $\tilde{B}(\pi 3s/3p/\sigma^*)$ state develops a clear CT character, with the π-type hole density being almost entirely localized on monomer b and the σ^*-type electron density localized completely on monomer a. The $\tilde{A}(\pi 3s/\sigma^*)$ state, on the other hand, develops a LE character, with the hole and particle densities being both localized on monomer a.

Further confirmation that the $\tilde{B}(\pi 3s/3p/\sigma^*)$ state develops a CT character as the N–H bond of monomer a is stretched is provided by the calculated exciton size and hole-electron distance for the $\tilde{B}(\pi 3s/3p/\sigma^*) \leftarrow \tilde{X}$ transition in the dissociation limit (N–H bond length of 4.3 a.u.) as a function of the intermonomer separation. These values are shown in Fig. 4. Both the exciton size and the electron-hole distance are found to increase linearly with the intermonomer separation. Particularly striking is the behavior of the exciton size, which takes on values very close to the intermonomer separation for all values considered. This analysis provides very strong evidence that the $\tilde{B}(\pi 3s/3p/\sigma^*)$ state develops an essentially pure CT character as the N–H bond of monomer a is stretched.

In order to explain the chosen character labels for the $\tilde{A}(\pi 3s/\sigma^*)$ and $\tilde{B}(\pi 3s/3p/\sigma^*)$ states, we consider the dominant NTOs for the $\tilde{A}(\pi 3s/\sigma^*) \leftarrow \tilde{X}$ and $\tilde{B}(\pi 3s/3p/\sigma^*) \leftarrow \tilde{X}$ transitions at the FC point and in the dissociation limit. These are shown in Fig. 5. At

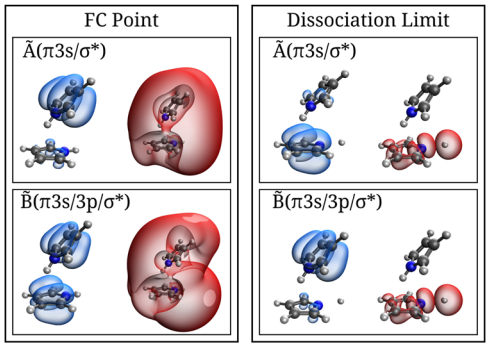

FIG. 3. Quasidiabatic hole (blue) and particle (red) densities for the $\tilde{A}(\pi 3s/\sigma^*)$ and $\tilde{B}(\pi 3s/3p/\sigma^*)$ states at the FC point and just within the dissociation limit. All densities were calculated at the DFT/MRCI/aug-cc-pVDZ level of theory.

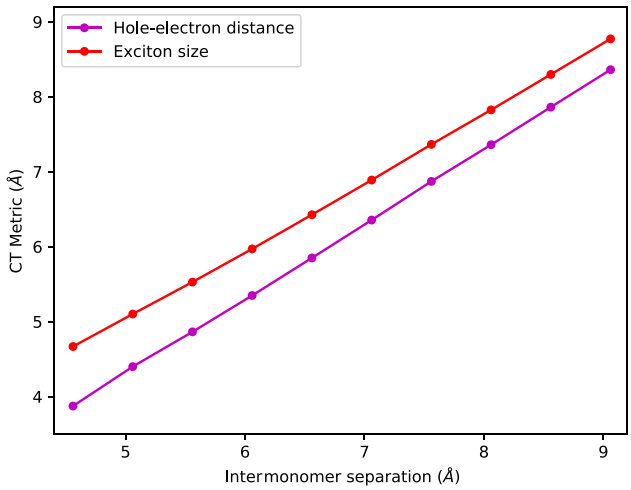

FIG. 4. Calculated exciton size and hole-electron distance for the $\tilde{B}(\pi 3s/3p/\sigma^*)$ state just within the dissociation limit as a function of the intermonomer separation. All calculations were performed at the DFT/MRCI/aug-cc-pVDZ level of theory.

Published under license by AIP Publishing

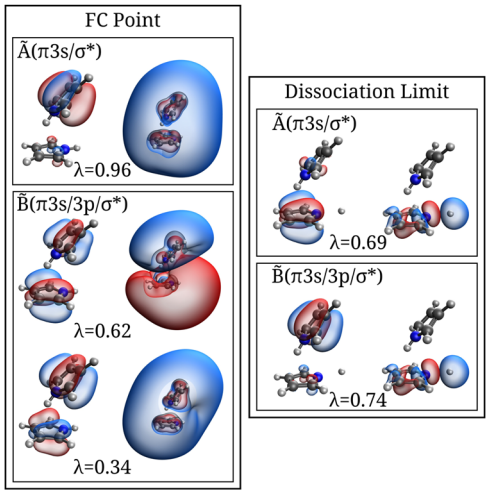

FIG. 5. Dominant quasidiabatic NTOs for the $\tilde{A}(\pi 3s/\sigma^*)$ and $\tilde{B}(\pi 3s/3p/\sigma^*)$ states at the FC point and just within the dissociation limit, calculated at the DFT/MRCI/aug-cc-pVDZ level of theory.

the FC point, the $\tilde{A}(\pi 3s/\sigma^*)$ state is clearly seen to correspond to a $\pi 3s$ state, while the $\tilde{B}(\pi 3s/3p/\sigma^*)$ state is found to be of mixed $\pi 3p$ and $\pi 3s$ characters. The NTOs in the dissociation limit clearly show the evolution of these states into LE- and CT-type $\pi\sigma^*$ states.

Two points here are worth making. First, we note that the evolution of the $\tilde{A}$ and $\tilde{B}$ states from the Rydberg to valence character as the free N–H bond of monomer *a* is broken is directly analogous to the change in the character of the $A_2(\pi 3s)$ and $B_1(\pi 3s)$ states of the monomer upon N–H dissociation. Second, this change in the character can be rationalized by assuming that the states involved are coupled to higher-lying states of $\pi\sigma^*$ character and that in the case of the $\tilde{B}(\pi 3s/3p/\sigma^*)$ state, this coupling drives electron transfer from monomer *b* to monomer *a*.

Finally, we note that the $\tilde{A}(\pi 3s/\sigma^*)$ and $\tilde{B}(\pi 3s/3p/\sigma^*)$ states were not found to evolve the CT character upon displacement of any of the projected normal modes $\bar{Q}_\alpha$. We thus conclude that the N–H dissociation is the primary mechanism by which electron transfer is mediated following photoexcitation.

C. Quantum dynamics simulations

In this section, we attempt to answer the question of whether the electron transfer pathway identified in Sec. III B is accessible following excitation to the $\tilde{A}/\tilde{B}$ state manifold and, if so, to what extent it can be expected to contribute to the excited state dynamics. This is achieved through the use of quantum dynamics calculations performed using the MCTDH method and the model potential described in Sec. II B.

1. Selection of dynamically active modes

To determine the relative dynamical importance of the projected normal modes $\bar{Q}_\alpha$, the dimensionless first-order coupling coefficients

$$\tilde{\kappa}_\alpha^{(\sigma)} = \frac{1}{\mathcal{W}_\alpha}\frac{\partial W_{\sigma\sigma}}{\partial \bar{Q}_\alpha}\bigg|_{\bar{\mathbf{Q}}=\mathbf{0}} \tag{14}$$

and

$$\tilde{\lambda}_\alpha^{(\sigma,\sigma')} = \frac{1}{\mathcal{W}_\alpha}\frac{\partial W_{\sigma\sigma'}}{\partial \bar{Q}_\alpha}\bigg|_{\bar{\mathbf{Q}}=\mathbf{0}} \tag{15}$$

are calculated. The values $-\tilde{\kappa}_\alpha^{(\sigma)}$ give the displacements of the minima of the quasidiabatic potentials from the reference point. The terms $\tilde{\lambda}_\alpha^{(\sigma,\sigma')}$ give a measure of the relative coupling interstate strengths of the projected normal modes $\bar{Q}_\alpha$. A total of 11 projected normal modes $\bar{Q}_\alpha$ were found to be of significant dynamical interest. These are $\bar{Q}_{10}$ (intermonomer bending), $\bar{Q}_{12}$ (monomer *a* out-of-plane bending), $\bar{Q}_{20}$ (monomer *b* C–H and N–H out-of-plane bending), $\bar{Q}_{28}$ (monomer *b* ring stretching), $\bar{Q}_{34}$ (monomer *b* C–H in-plane bending), $\bar{Q}_{35}$ (monomer *a* C–H in-plane bending), $\bar{Q}_{38}$ (monomer *b* ring breathing), $\bar{Q}_{42}$ (monomer *a* C–H in-plane bending), $\bar{Q}_{43}$ (monomer *a* C–C stretching), $\bar{Q}_{46}$ (monomer *b* C–N–C stretching), and $\bar{Q}_{49}$ (monomer *a* C–N–C stretching). These modes, together with the monomer *a* N–H stretching coordinate, $\bar{r}$, were included in the MCTDH quantum dynamics simulation. That is, a two-state [$\tilde{A}(\pi 3s/\sigma^*)$ and $\tilde{B}(\pi 3s/3p/\sigma^*)$], twelve-mode model was used. A propagation time of 300 fs was used, and the mode combination scheme and numbers of basis functions used are given in Table II.

Finally, we note that the monomerization coordinate $\bar{R}$ was not included in the MCTDH calculations even though our previous work had suggested that this coordinate was a potentially dynamically important mode.[25] Indeed, as shown in Fig. 2, the excited state adiabatic potentials along this nuclear degree of freedom are predicted to be either very weakly bound or dissociative for the S_1 and S_2 states, respectively. However, we are interested in the short time dynamics occurring during the first few hundred femtoseconds following excitation to the $\tilde{A}(\pi 3s/\sigma^*)$ and $\tilde{B}(\pi 3s/3p/\sigma^*)$ states, and the N–H dissociation dynamics in particular. Due to the differences in frequencies between the two nuclear coordinates, it can be expected that N–H dissociation will occur on a much faster time scale than dissociation into monomers. Then, given the necessary use of a complex absorbing potential (CAP) for the N–H dissociation coordinate $\bar{r}$ (see Appendix D), the excited state wavepacket

TABLE II. Computational details of the wavepacket propagations corresponding to excitation to the $\tilde{A}(\pi 3s/\sigma^*)$ and $\tilde{B}(\pi 3s/3p/\sigma^*)$ states. The DVR types exp and HO correspond to exponential and harmonic oscillator DVRs, respectively. N_i and N_j are the number of primitive DVR functions used to describe each combined mode. n_i are the number of single-particle functions used for each state. For the coordinate $\bar{r}$, the exp DVR grid ran from $\bar{r} = -5$ to $\bar{r} = 25$.

Combined mode	DVR type	N_i, N_j	$n_{\tilde{A}(\pi 3s/\sigma^*)}, n_{\tilde{B}(\pi 3s/3p/\sigma^*)}$
$(\bar{Q}_{10}, \bar{r})$	HO, exp	17,71	10,11
$(\bar{Q}_{28}, \bar{Q}_{35})$	HO, HO	12,17	12,10
$(\bar{Q}_{38}, \bar{Q}_{42})$	HO, HO	17,35	8,12
$(\bar{Q}_{12}, \bar{Q}_{46})$	HO, HO	17,13	12,10
$(\bar{Q}_{20}, \bar{Q}_{34})$	HO, HO	10,15	12,9
$(\bar{Q}_{43}, \bar{Q}_{49})$	HO, HO	35,13	9,10

Published under license by AIP Publishing

may be expected to be all but completely annihilated by the time that motion along the monomerization coordinate $\tilde{R}$ begins to occur. To determine estimates for the time scales for monomerization, numerically exact one-dimensional wavepacket propagations were performed with initial states corresponding to vertical excitation to the $\tilde{A}(\pi 3s/\sigma^*)$ and $\tilde{B}(\pi 3s/3p/\sigma^*)$ states. The details of these calculations are given in Appendix F. The computed nuclear densities are shown in Fig. 6 as a function of the change in the intermonomer separation relative to the time $t = 0$ expectation value. For the $\tilde{A}(\pi 3s/\sigma^*)$ state, the vertically excited wavepacket remains bound and undergoes small amplitude motion on a 600 fs time scale. For excitation to the $\tilde{B}(\pi 3s/3p/\sigma^*)$ state, dissociation into monomers is predicted to occur, albeit on a long (several hundred femtosecond) time scale. Given the small displacements along the coordinate $\tilde{R}$ occurring within the first 300 fs, we conclude that the exclusion of this degree of freedom from the MCTDH calculations is acceptable given the much faster time scale for N–H dissociation, as will be discussed in Secs. III C 2 and III C 3.

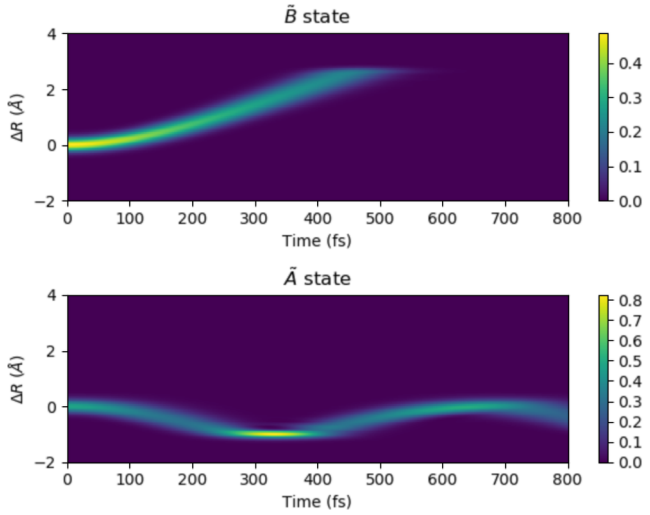

FIG. 6. Densities for the coordinate R calculated following vertical excitation to the $\tilde{A}(\pi 3s/\sigma^*)$ and $\tilde{B}(\pi 3s/3p/\sigma^*)$ states using a numerically exact one-dimensional wavepacket propagation.

2. Dynamics following excitation to the $\tilde{A}(\pi 3s/\sigma^*)$ state

In Fig. 7(a) are shown the quasidiabatic state populations calculated following vertical excitation to the $\tilde{A}(\pi 3s/\sigma^*)$ state. Overall, most of the population is predicted to remain in the initially excited $\tilde{A}(\pi 3s/\sigma^*)$ state, with $\tilde{A}(\pi 3s/\sigma^*)$ and $\tilde{B}(\pi 3s/3p/\sigma^*)$ state populations of 0.73 and 0.27, respectively, after 300 fs. Of the 27% of the population transferred to the $\tilde{B}(\pi 3s/3p/\sigma^*)$ state, the majority (22%) is transferred within the first 10 fs.

We next consider the N–H dissociation dynamics following excitation to the $\tilde{A}(\pi 3s/\sigma^*)$ state. Shown in Fig. 8(a) are the calculated state-resolved fluxes for dissociation following vertical excitation to this state. Additionally, in Fig. 9(a), we show the total and state-resolved probabilities of N–H dissociation. By the end of the 300 fs propagation time, the total calculated probability of dissociation is 0.34. That is, the N–H dissociation pathway is predicted to be open following excitation to the $\tilde{A}(\pi 3s/\sigma^*)$ state but not dominant. The state-resolved probabilities of dissociation in the $\tilde{A}(\pi 3s/\sigma^*)$ and $\tilde{B}(\pi 3s/3p/\sigma^*)$ states are 0.13 and 0.21, respectively. That is, we predict a branching ratio between dissociation in the $\tilde{A}(\pi 3s/\sigma^*)$ and $\tilde{B}(\pi 3s/3p/\sigma^*)$ states of 1.62. The exciton-based analysis of the $\tilde{B}(\pi 3s/3p/\sigma^*)$ state wavefunction presented in Sec. III B (b) suggests that it develops a strong CT character as the monomer a N–H bond is stretched. We can thus postulate that the quantum yield for electron transfer from monomer b to monomer a will be comparable to that for N–H dissociation in the $\tilde{B}(\pi 3s/3p/\sigma^*)$ state. This, coupled with the calculated probabilities for N–H dissociation, then suggests that electron transfer may be an open relaxation pathway

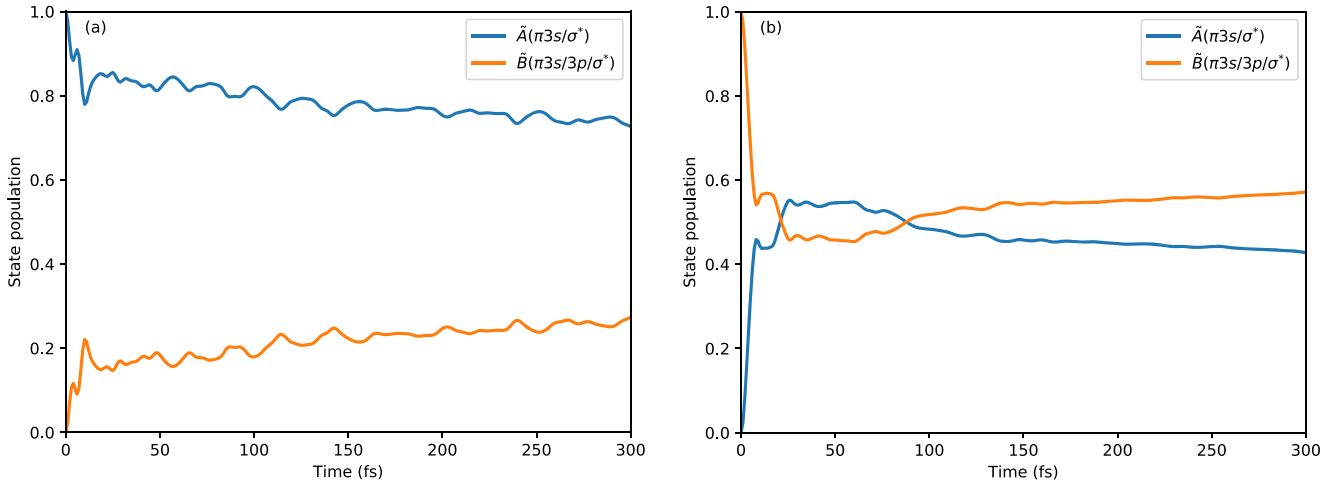

FIG. 7. Calculated quasidiabatic state populations following vertical excitation to (a) the $\tilde{A}(\pi 3s/\sigma^*)$ state and (b) the $\tilde{B}(\pi 3s/3p/\sigma^*)$ state.

Published under license by AIP Publishing

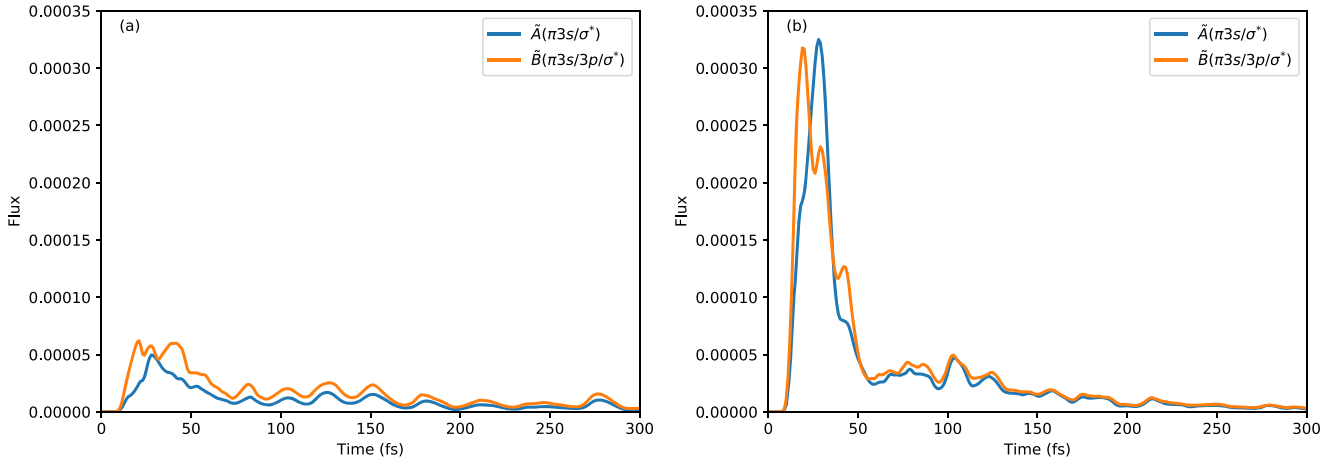

FIG. 8. Calculated quasidiabatic state-resolved flux along the N–H dissociation coordinate *r* following vertical excitation to (a) the $\tilde{A}(\pi 3s/\sigma^*)$ state and (b) the $\tilde{B}(\pi 3s/3p/\sigma^*)$ state.

following excitation to the $\tilde{A}(\pi 3s/\sigma^*)$ state although not the dominant one.

3. Dynamics following excitation to the $\tilde{B}(\pi 3s/3p/\sigma^*)$ state

Shown in Fig. 7(b) are the quasidiabatic state populations calculated following vertical excitation to the $\tilde{B}(\pi 3s/3p/\sigma^*)$ state. A period of rapid internal conversion to the $\tilde{A}(\pi 3s/\sigma^*)$ state is predicted to exist, the population of which peaks at a value of 0.55 at around 25 fs. At the end of the 300 fs propagation, the values of the $\tilde{A}(\pi 3s/\sigma^*)$ and $\tilde{B}(\pi 3s/3p/\sigma^*)$ state populations are 0.43 and 0.57, respectively.

Shown in Fig. 8(b) are the calculated state-resolved fluxes for dissociation in each of the $\tilde{A}(\pi 3s/\sigma^*)$ and $\tilde{B}(\pi 3s/3p/\sigma^*)$ states. In Fig. 9(b), we show the state-resolved and total N–H dissociation probabilities. It is predicted that ultrafast N–H dissociation will occur following excitation to the $\tilde{B}(\pi 3s/3p/\sigma^*)$ state, with total dissociation probabilities of 0.56 at 50 fs and 0.92 by 300 fs. Dissociation is predicted to occur in both the initially excited $\tilde{B}(\pi 3s/3p/\sigma^*)$ and $\tilde{A}(\pi 3s/\sigma^*)$ states, with a $\tilde{B}(\pi 3s/3p/\sigma^*)/\tilde{A}(\pi 3s/\sigma^*)$ branching ratio of 1.49. Taking the probability of dissociation in the $\tilde{B}(\pi 3s/3p/\sigma^*)$ state to be proportional to the quantum yield for electron transfer, we thus conclude the probability of electron transfer from monomer *b* to monomer *a* following vertical excitation to the $\tilde{B}(\pi 3s/3p/\sigma^*)$ state to be high.

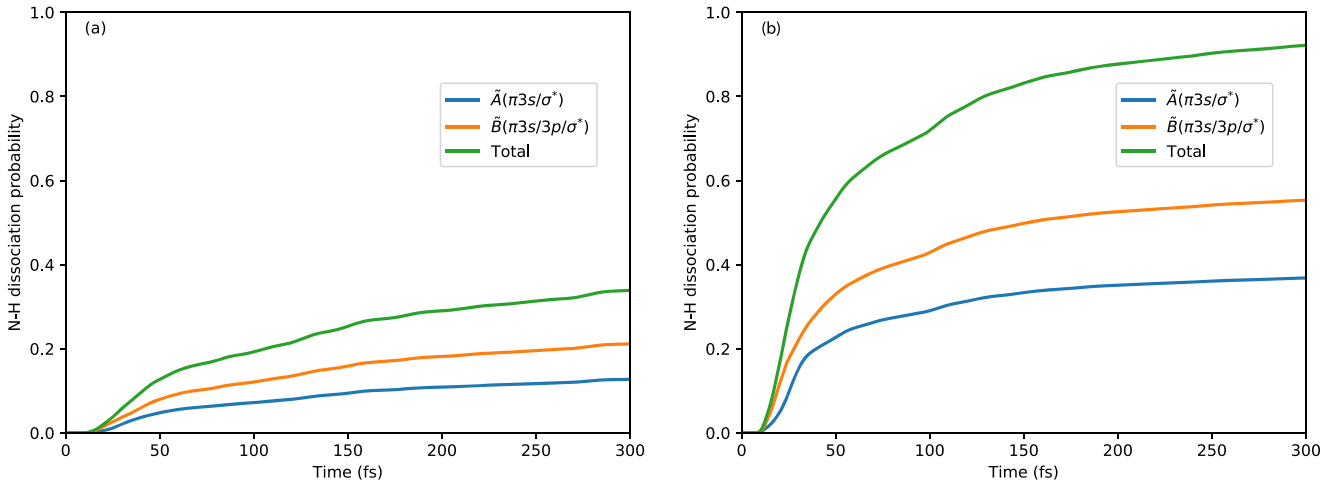

FIG. 9. Calculated quasidiabatic state-resolved N–H dissociation probabilities coordinate following vertical excitation to (a) the $\tilde{A}(\pi 3s/\sigma^*)$ state and (ii) the $\tilde{B}(\pi 3s/3p/\sigma^*)$ state.

Published under license by AIP Publishing

IV. DISCUSSION

We here collect together the results of our electronic structure theory calculations and quantum dynamics simulations and consider their interpretation in connection to previous studies of the excited-state dynamics of the pyrrole dimer.

First, we note that our exciton-based analysis of the $\tilde{A}(\pi 3s/\sigma^*)$ and $\tilde{B}(\pi 3s/3p/\sigma^*)$ states sheds new light on the nature of their electronic characters. Our calculations predict that the $\tilde{A}(\pi 3s/\sigma^*)$ state has a delocalized $\pi 3s$ Rydberg character at the FC point, while the $\tilde{B}(\pi 3s/3p/\sigma^*)$ state is of a mixed $\pi 3s/\pi 3p$ character at this geometry. Upon stretching of the N–H bond of monomer *a*, both states are found to develop a pure $\pi\sigma^*$ valence character due to vibronic coupling to higher-lying $\pi\sigma^*$ states. In the case of the $\tilde{A}(\pi 3s/\sigma^*)$ state, the LE electronic character develops, with both the π-type hole and σ^*-type electron densities being localized on monomer *a*. For the $\tilde{B}(\pi 3s/3p/\sigma^*)$ state, on the other hand, the electronic character is found to evolve to one of the pure CT character, with the hole and electron densities being localized on monomer *b* and monomer *a*, respectively.

We note that these assignments are at odds with those made in Ref. 25, which assigned CT character to the $\tilde{A}(\pi 3s/\sigma^*)$ state at the FC point based on a simple MO analysis, highlighting the need for electronic state analyses beyond the uncorrelated one-electron basis function level. Given the increased rigor of exciton-based analysis presented here, we are inclined to favor these reassignments.

Second, we consider the excited-state relaxation pathways predicted to be open following excitation to the $\tilde{A}(\pi 3s/\sigma^*)$ and $\tilde{B}(\pi 3s/3p/\sigma^*)$ states. In both cases, our quantum dynamics simulations predict that an electron transfer pathway driven by N–H dissociation in the $\tilde{B}(\pi 3s/3p/\sigma^*)$ state will be open. In the case of excitation to the $\tilde{A}(\pi 3s/\sigma^*)$ state, this is predicted to be a relatively minor pathway. Conversely, following excitation to the $\tilde{B}(\pi 3s/3p/\sigma^*)$ state, we predict this to be the dominant relaxation pathway. Here, it is worth comparing our calculations, where possible, to previous experimental results. Two previous studies have probed the dynamics of the pyrrole dimer following excitation using photon energies that should result predominantly in population of the $\tilde{B}(\pi 3s/3p/\sigma^*)$.[25,26]

In the TRPES study of Fielding and co-workers,[25] excitation of nonsize-selected mixtures of pyrrole homoclusters at a photon energy of 5.17 eV was found to give rise to two time constants attributable to the excited state dynamics of the pyrrole dimer. These comprised a fast time constant, $\tau_1 = 46 \pm 8$ fs, and a slow time constant, $\tau_2 = 190 \pm 30$ fs. The fast time constant was attributed to the flow of population of the initially excited $\tilde{B}(\pi 3s/3p/\sigma^*)$ state into the $\tilde{A}(\pi 3s/\sigma^*)$ state, and the slow time constant was taken to correspond to dissociation in the $\tilde{A}(\pi 3s/\sigma^*)$ state.

In the size-selected time-resolved ion imaging study of Montero *et al.*,[26] a lifetime of $\tau = 270 \pm 19$ fs was determined for the excited state population following excitation at 5.10 eV.

While our calculations cannot provide a direct comparison to these experimental measurements, we can make an indirect comparison if we assume that N–H dissociation was the primary mechanism by which the wavepacket moves out of the ionization window in the experimental studies. This may be deemed a reasonable approximation due to the high frequency of the N–H stretching coordinate in comparison with the other modes.

Furthermore, in the experimental studies being compared to, the sums of the pump and probe photon energies were low enough that only the FC region could be probed. Making this assumption, we may then use the population of the subspace of nuclear configurations corresponding to a bound N–H bond as a proxy for the population of the ionization window. For this purpose, we consider the state-resolved expectation values of the projector onto the interaction region,

$$p_I^{(\sigma)}(t) = \langle \Psi(t)|\Phi_\sigma\rangle\langle\Phi_\sigma|\Theta(r_d - r)|\Phi_\sigma\rangle\langle\Phi_\sigma|\Psi(t)\rangle, \qquad (16)$$

where $\Theta(r_d - r)$ is the reverse Heaviside step function centered at an N–H bond length r_d. The expectation value $p_I^{(\sigma)}$ gives a measure of the proportion of the population in the state $|\Phi_\sigma\rangle$ that is in the subspace for which $r < r_d$. Choosing a value of r_d that corresponds to an N–H bond length just within the asymptotic region of the potential (here taken as 4.7 a.u.), $p_I^{(\sigma)}$, provides a measure of the population in the state $|\Phi_\sigma\rangle$ that has not yet reached the dissociation limit. Hence, $p_I^{(\sigma)}$ provides our proxy for the probability of remaining within the ionization window of the experiments of Refs. 25 and 26.

Shown in Fig. 10 are the calculated values of $p_I^{(\sigma)}$ following excitation to the $\tilde{B}(\pi 3s/3p/\sigma^*)$ state. By fitting to monoexponential functions, we determine a time scale of 23 fs for the decay of $\tilde{B}(\pi 3s/3p/\sigma^*)$ state interaction region population, both due to dissociation in this state and internal conversion to the $\tilde{A}(\pi 3s/\sigma^*)$ state. The $\tilde{A}(\pi 3s/\sigma^*)$ state interaction region population is found to reach its maximum value at 24 fs and then subsequently decay on a time scale of 100 fs. We note, with the caveat that they are only indirectly comparable, that these calculated time scales are found to compare quite well with the time constants extracted from the TRPES study of Fielding *et al.* for decay of the initially excited $\tilde{B}(\pi 3s/3p/\sigma^*)$ state and the subsequent decay of the $\tilde{A}(\pi 3s/\sigma^*)$ state. The excited state lifetime of $\tau = 270 \pm 19$ fs reported by Montero *et al.* is longer

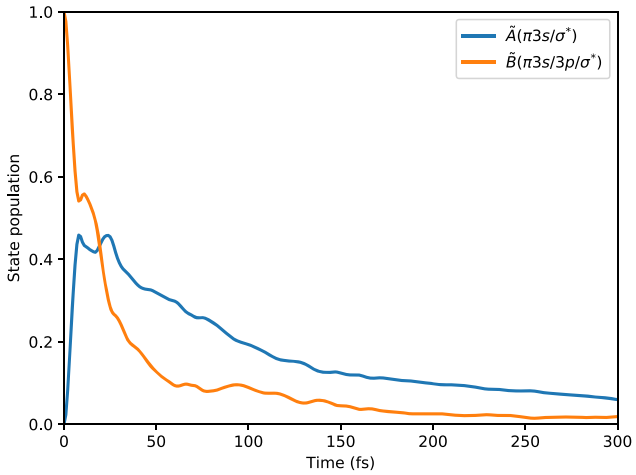

FIG. 10. Calculated quasidiabatic state-resolved interaction region populations following vertical excitation to the $\tilde{B}(\pi 3s/3p/\sigma^*)$ state.

Published under license by AIP Publishing

than our calculated time scale for N–H dissociation following vertical excitation to the $\tilde{B}(\pi 3s/3p/\sigma^*)$ state, although they are both of the order of 100 fs. We note, however, that the spectrum of vibronic states prepared by vertical excitation will be much broader than that prepared via interaction with a femtosecond pump pulse, which may help to explain this discrepancy.

V. CONCLUSIONS

The photoinduced dynamics of heteroaromatic dimers can be anticipated to differ substantially from those of the constituent monomers. In particular, both delocalized and CT-type states may exist in the dimer species in addition to monomer-type LE states. The role of delocalized and CT-type states in the excited-state dynamics of heteroaromatic dimers has, however, not previously been the subject of any in-depth theoretical studies. As a first step toward this, in this work, we have presented a detailed study of electron transfer in photoexcited pyrrole dimers using both electronic structure theory calculations and quantum dynamics simulations.

Using an exciton-based analysis at the DFT/MRCI level of theory, we have analyzed the electronic characters of the $\tilde{A}(\pi 3s/\sigma^*)$ and $\tilde{B}(\pi 3s/3p/\sigma^*)$ states of the pyrrole dimer. These calculations revealed clearly that both states possess a delocalized Rydberg character within the FC region but, due to vibronic coupling to a higher-lying states, acquire a valence character as the N–H bond of monomer *a* is stretched. In the case of the $\tilde{A}(\pi 3s/\sigma^*)$ state, the evolution is to a locally excited $\pi\sigma^*$ character. On the other hand, the $\tilde{B}(\pi 3s/3p/\sigma^*)$ state is found to acquire a distinct CT character as the N–H bond is elongated. Through this, an electron transfer pathway is accessible following electronic excitation. Additionally, using a newly developed model Hamiltonian parameterized by fitting to DFT/MRCI energies, quantum dynamics simulations of the pyrrole dimer excited to the $\tilde{A}(\pi 3s/\sigma^*)$ and $\tilde{B}(\pi 3s/3p/\sigma^*)$ states were performed using the MCTDH method. The results of these simulations suggest that the abovementioned electron transfer pathway will be open following excitation to both states and may be the dominant relaxation pathway following excitation to the $\tilde{B}(\pi 3s/3p/\sigma^*)$ state.

Finally, we note that there are some interesting similarities that may be drawn between the excited-state dynamics of the pyrrole dimer and that of dinucleotide species. In particular, the evolution of the $\tilde{B}(\pi 3s/3p/\sigma^*)$ excited state wavepacket from the delocalized to CT character is somewhat analogous to the observed dynamics in photoexcited π-stacked dinucleotides.[28] This, combined with the rigorous levels of electronic structure and quantum dynamics theory that may be brought to bear on them, makes the study of photoexcited small heteroaromatic dimers an appealing field of research.

SUPPLEMENTARY MATERIAL

The model Hamiltonians used in the quantum dynamics simulations are provided in the supplementary material in the form of Quantics operator files. Additionally, the projected normal modes $\tilde{q}_\alpha$ are also given in the xyz format in terms of nonweighted Cartesian coordinates for the purpose of visual inspection.

APPENDIX A: DEFINITION OF THE PROJECTED NORMAL MODES

Let $\boldsymbol{H}$ denote the mass-weighted ground state Hessian,

$$H_{ij} = \frac{1}{\sqrt{m_i m_j}} \frac{\partial^2 V_0}{\partial x_i \partial x_j}. \tag{A1}$$

Here, V_0 denotes the ground state potential, and the x_i are the Cartesian coordinates. The projected mass-weighted Hessian, $\boldsymbol{\mathcal{H}}$, is then defined as

$$\boldsymbol{\mathcal{H}} = (\mathbf{1} - \boldsymbol{P})\boldsymbol{H}(\mathbf{1} - \boldsymbol{P}), \tag{A2}$$

where $\boldsymbol{P}$ denotes the projector, in terms of mass-weighted Cartesians, onto the space spanned by the coordinates r and R,

$$\boldsymbol{P} = \tilde{\boldsymbol{r}} \otimes \tilde{\boldsymbol{r}} + \tilde{\boldsymbol{R}} \otimes \tilde{\boldsymbol{R}}, \tag{A3}$$

where $\{\tilde{r}_i\} = \{\sqrt{m_i} r_i\}$, and $\{\tilde{R}_i = \sqrt{m_i} R_i\}$ are the mass-weighted vectors corresponding to the coordinates r and R. $\boldsymbol{\mathcal{H}}$ is then diagonalized,

$$\boldsymbol{\mathcal{H}} = \boldsymbol{U}^T \boldsymbol{\Omega} \boldsymbol{U}, \tag{A4}$$

yielding the eigenvector and eigenvalue matrices $\boldsymbol{U}$ and $\boldsymbol{\Omega}$, respectively. The projected normal modes $\tilde{q}_\alpha$ are obtained from the $3N - 2$ eigenvectors with nonzero eigenvalues. That is, taking the eigenvectors to be arranged in order of increasing eigenvalue,

$$\tilde{q}_{\alpha-2} = \sum_{i=1}^{3N} U_{\alpha i} \tilde{x}_i, \quad \alpha = 3, \ldots, 3N - 2. \tag{A5}$$

Using the projected normal modes $\tilde{q}_\alpha$ together with the lengths, $\tilde{r}$ and $\tilde{R}$, of the vectors $\tilde{\boldsymbol{r}}$ and $\tilde{\boldsymbol{R}}$, we arrive at a set of nuclear coordinates suitable for the description of the excited state dynamics of the pyrrole dimer.

It remains to be noted that the set of nuclear coordinates $\{\tilde{r}, \tilde{R}, \tilde{q}_\alpha : \alpha = 1, \ldots, 3N - 2\}$ is not orthogonal to the subspace of center-of-mass translations and infinitesimal rotations. The decision not to project out these zero-frequency modes was a compromise made in order to be able to define single coordinates corresponding to N–H stretching and dissociation into monomers, that is, $\tilde{r}$ and $\tilde{R}$. We note, however, that the subset of dynamically active coordinates chosen for inclusion in the quantum dynamics calculations (discussed in Sec. II B) was found to have a minimal overlap with the modes spanning the translation-rotation subspace. As such, we consider this to be an acceptable coordinate construction procedure.

APPENDIX B: THE MODEL DIABATIC POTENTIAL

The subsystem potential for the bound degrees of freedom $\tilde{Q}_\alpha$ is taken as a truncated second-order vibronic coupling Hamiltonian. Collecting terms of the same order. We write this as

$$\boldsymbol{W}(\tilde{\boldsymbol{Q}}) = \boldsymbol{W}^{(0)}(\tilde{\boldsymbol{Q}}) + \boldsymbol{W}^{(1)}(\tilde{\boldsymbol{Q}}) + \boldsymbol{W}^{(2)}(\tilde{\boldsymbol{Q}}). \tag{B1}$$

The zeroth-, first-, and second-order potentials read

Published under license by AIP Publishing

$$W^{(0)}_{\sigma\sigma'}(\bar{\mathbf{Q}}) = \left(E_\sigma + \frac{1}{2}\sum_{\alpha=1}^{3N-2}\mathcal{W}_\alpha \bar{Q}^2_\alpha\right)\delta_{\sigma\sigma'}, \tag{B2}$$

$$W^{(1)}_{\sigma\sigma}(\bar{\mathbf{Q}}) = \sum_{\alpha=1}^{3N-2}\kappa^{(\sigma)}_\alpha \bar{Q}_\alpha, \tag{B3}$$

$$W^{(1)}_{\sigma\sigma'}(\bar{\mathbf{Q}}) = \sum_{\alpha=1}^{3N-2}\lambda^{(\sigma,\sigma')}_\alpha \bar{Q}_\alpha, \quad \sigma \neq \sigma', \tag{B4}$$

$$W^{(2)}_{\sigma\sigma}(\bar{\mathbf{Q}}) = \frac{1}{2}\sum_{\alpha=1}^{3N-2}\gamma^{(\sigma)}_{\alpha\alpha}\bar{Q}^2_\alpha. \tag{B5}$$

Here, the zeroth-order potential corresponds to the set of projected normal mode harmonic oscillators displaced by the reference geometry vertical excitation energies E_σ. Note that we neglect the interstate coupling terms as well as the bilinear intrastate coupling terms in the second-order potential $\boldsymbol{W}^{(2)}(\bar{\mathbf{Q}})$.

The uncorrelated contributions from the unbound coordinates $\bar{r}$ and $\bar{R}$ were taken as functions exhibiting the correct asymptotic behaviors. Specifically, we modeled the on-diagonal elements of the quasidiabatic potential with respect to these two degrees of freedom as avoided-crossing potentials with the following functional form:

$$W_{\sigma\sigma}(X) = \frac{1}{2}\left(v^{(\sigma)}_b(X) + v^{(\sigma)}_d(X) - \sqrt{\left[v^{(\sigma)}_b(X) - v^{(\sigma)}_d(X)\right]^2 + 4\left[a^{(\sigma)}_X \tanh\left(b^{(\sigma)}_X X\right)\right]^2}\right), \tag{B6}$$

$$X = \bar{r}, \bar{R},$$

with

$$v^{(\sigma)}_b(X) = D^{(\sigma)}_{Xb}\left(1 - \exp\left(-\alpha^{(\sigma)}_{Xb}\left[X - X^{(\sigma)}_{0b}\right]\right)\right)^2, \tag{B7}$$

$$v^{(\sigma)}_d(X) = A^{(\sigma)}_X \exp\left(-\alpha^{(\sigma)}_{Xd}\left[X - X^{(\sigma)}_{0d}\right]\right) + D^{(\sigma)}_{Xd}. \tag{B8}$$

The coupling between the $\tilde{A}(\pi 3s/\sigma^*)$ and $\tilde{B}(\pi 3s/3p/\sigma^*)$ states by the coordinates $\bar{r}$ and $\bar{R}$ was taken to assume the following hyperbolic tangent form:

$$W_{12}(X) = S_X \tanh(G_X X), \quad X = \bar{r}, \bar{R}. \tag{B9}$$

The correlation between the bound degrees of freedom $\bar{Q}_\alpha$ and the dissociative N–H dissociation coordinate $\bar{r}$ was dealt with by taking the first-order coupling coefficients $\kappa^{(\sigma)}_\alpha$ and $\lambda^{(\sigma,\sigma')}_\alpha$ that enter into the subsystem potential $\boldsymbol{W}(\bar{\mathbf{Q}})$ to be functions of $\bar{r}$ with the correct asymptotic form. This was achieved by the use of the following interaction potential $\boldsymbol{W}^{(int)}(\bar{r}, \bar{\boldsymbol{q}})$:

$$W^{(int)}_{\sigma\sigma}(\bar{r}, \bar{\mathbf{Q}}) = \sum_{\alpha=1}^{3N-2} K^{(\sigma)}_{1\alpha}\tanh\left(K^{(\sigma)}_{2\alpha}\bar{r}\right)\bar{Q}_\alpha, \tag{B10}$$

$$W^{(int)}_{\sigma\sigma'}(\bar{r}, \bar{\mathbf{Q}}) = \sum_{\alpha=1}^{3N-2} \Lambda^{(\sigma,\sigma')}_{1\alpha}\tanh\left(\Lambda^{(\sigma,\sigma')}_{2\alpha}\bar{r}\right)\bar{Q}_\alpha, \quad \sigma \neq \sigma'. \tag{B11}$$

Here, the parameters $K^{(\sigma)}_{i\alpha}$ correspond to the change in the quasidiabatic state minima with respect to the projected normal modes $\bar{Q}_\alpha$ as the N–H bond dissociates. Similarly, the parameters $\Lambda^{(\sigma,\sigma')}_{i\alpha}$ describe the changes in the nonadiabatic coupling by the projected normal modes as the N–H bond is broken.

APPENDIX C: PARAMETERIZATION OF THE MODEL DIABATIC POTENTIAL

The projected normal modes $\bar{Q}_\alpha$ and frequencies $\mathcal{W}_\alpha$ were calculated at the spin-component scaled MP2 (SCS-MP2) level of theory using the Turbomole set of programs.[44]

The remaining parameters of the model potential were determined via the minimization of the root mean square deviation (RMSD) of the model adiabatic energies from the adiabatic energies calculated at a number of nuclear geometries at the DFT/MRCI/aug-cc-pVDZ level of theory. This was achieved using the VCHAM set of programs, which form a part of the Quantics quantum dynamics package.[34] In order for the model potential to be preferentially accurate in the lower-energy regions of nuclear configuration space sampled by the excited-state wavepacket, the following weighted functional was optimized:

$$\Delta = \sum_\sigma\sum_{i=1}^{n_\sigma}\left(V^\sigma_i - V^{\sigma,mod}_i\right)^2 w^\sigma_i. \tag{C1}$$

Here, n_σ is the number of fitting geometries used for the σth electronic state, and V^σ_i and $V^{\sigma,mod}_i$ are the true and model adiabatic energies at the ith geometry for the σth state, respectively. w^σ_i is a weight function, chosen as

$$w^\sigma_i = \exp\left(-\left(V^\sigma_i - V^\sigma_0\right)\right), \tag{C2}$$

where V^σ_0 is the value of the σth adiabatic potential at the reference geometry.

For the bound modes $\bar{Q}_\alpha$, initial guesses for the values of the first-order coupling coefficients $\kappa^{(\sigma)}_\alpha$ and $\lambda^{(\sigma,\sigma')}_\alpha$ were calculated analytically at the multireference first-order configuration interaction (MR-FOCI) level of theory using the aug-cc-pVDZ basis. These calculations employed an (8,8) active space comprised of the four occupied orbitals: $23a'(\pi_A)$, $24a'(\pi_A)$, $13a''(\pi_B)$, and $14a''(\pi_A)$, and the four virtual orbitals: $23a'(3s_A)$, $34a'(3p_{z,A})$, $25a'(\pi^*_A)$, and $15a''(\pi^*_A)$. The MR-FOCI calculations were performed using the COLUMBUS suite of programs.[45]

Particularly careful attention was paid to the parameterization of the subsystem potential $\boldsymbol{W}(\bar{r})$ for the N–H dissociation coordinate $\bar{r}$. The avoided crossing model potential [Eq. (B6)] used to model the quasidiabatic potentials along the N–H dissociation coordinate $\bar{r}$ is extremely flexible. So much so, in fact, that it is capable of reproducing the adiabatic potentials along $\bar{r}$ even if the coupling between the $\tilde{A}(\pi 3s/\sigma^*)$ and $\tilde{B}(\pi 3s/3p/\sigma^*)$ states is completely neglected. This means that there is the strong possibility that the fitting procedure used will produce an excellent fit to the calculated adiabatic potentials but fail to correctly describe the coupling of the $\tilde{A}(\pi 3s/\sigma^*)$ and $\tilde{B}(\pi 3s/3p/\sigma^*)$ states by the coordinate $\bar{r}$. To avoid

Published under license by AIP Publishing

this, the parameters of the subsystem potential $W(\tilde{r})$ were fitted in a three-step procedure. First, the interstate coupling was taken as a first-order expansion, with the coupling coefficient held fixed at the value yielded by the initial-value generating MR-FOCI calculation, and the on-diagonal potential parameters optimized by fitting to the DFT/MRCI energies. Next, the interstate coupling function was set to the hyperbolic tangent form given in Eq. (B9). Initial values of the parameters $S_{\tilde{r}}$ and $G_{\tilde{r}}$ were set to reproduce the gradient of $W_{12}(\tilde{r})$ calculated at the MR-FOCI level of theory. These two parameters were then optimized with the intrastate parameters frozen at the values determined in the first step. Finally, all parameters were re-optimized using the output of the first and second steps as input. This procedure yielded an excellent fit to the calculated DFT/MRCI adiabatic potentials while also reproducing the MR-FOCI determined gradient of $W_{12}(\tilde{r})$.

APPENDIX D: MCTDH CALCULATIONS

In the MCTDH calculations, the so-called multiset formalism was used, in which the wavefunction ansatz reads

$$|\Psi(\boldsymbol{q},t)\rangle = \sum_{\sigma=1}^{n_s} |\Phi_\sigma\rangle \left|\Psi^{(\sigma)}(\boldsymbol{q},t)\right\rangle. \tag{D1}$$

Here, σ indexes the electronic states $|\Phi_\sigma\rangle$, and $\left|\Psi^{(\sigma)}(\boldsymbol{q},t)\right\rangle$ is the nuclear wavefunction for the σth electronic state. Each nuclear wavefunction $\left|\Psi^{(\sigma)}(\boldsymbol{q},t)\right\rangle$ is expanded in a direct product basis formed from time-dependent functions $\varphi_{j_k^\sigma}^{(\kappa,\sigma)}$, termed single-particle functions (SPFs),

$$\left|\Psi^{(\sigma)}(\boldsymbol{q},t)\right\rangle = \sum_{j_1^\sigma=1}^{n_1^\sigma} \cdots \sum_{j_p^\sigma=p}^{n_p^\sigma} A_{j_1^\sigma,\ldots,j_p^\sigma}^{(\sigma)}(t) \prod_{\kappa=1}^{p} \varphi_{j_\kappa^\sigma}^{(\kappa,\sigma)}(q_\kappa,t). \tag{D2}$$

The SPFs are functions of generally multidimensional logical coordinates q_κ, each corresponding to a composite of d_κ physical nuclear coordinates $Q_\nu^{(\kappa)}$,

$$q_\kappa = \left(Q_1^{(\kappa)},\ldots,Q_{d_\kappa}^{(\kappa)}\right). \tag{D3}$$

The time-dependent SPFs are further expanded in terms of a time-independent discrete variable representation (DVR).[32,42] Equations of motion for both the expansion coefficients $A_{j_1^\sigma,\ldots,j_p^\sigma}^{(\sigma)}$ and the SPFs are derived variationally, yielding an optimal description of the evolving wavepacket.[32]

In order to avoid the use of a prohibitively long DVR grid for the dissociative degree of freedom $\tilde{r}$, the Hamiltonian was augmented with a CAP, denoted by $\theta(\tilde{r})$,

$$\hat{H} \to \hat{H} + \sum_{\sigma=1}^{n_s} |\Phi_\sigma\rangle\theta(\tilde{r})\langle\Phi_\sigma|, \tag{D4}$$

where

$$\theta(\tilde{r}) = -i\eta\Theta(\tilde{r}-\tilde{r}_c)(\tilde{r}-\tilde{r}_c)^m. \tag{D5}$$

Here, η denotes a strength parameter, and $\Theta(\tilde{r}-\tilde{r}_c)$ denotes the Heaviside step function centered at $\tilde{r}_c$. With a suitably chosen strength η and order m, a CAP placed sufficiently far into the asymptotic region of the potential will annihilate those components entering into it before the edge of the grid is reached. In all wavepacket propagations, CAP parameters of $\eta = 0.005$, $\tilde{r}_c = 15.0$, and $m = 3$ were used.

APPENDIX E: CALCULATION OF DISSOCIATION YIELDS

We define the probability of dissociation of the N–H bond of monomer a at time t, $p_d(t)$, as the expectation value of the projector onto the subspace for which $\tilde{r} > \tilde{r}_d$, where $\tilde{r}_d$ corresponds to a bond length within the asymptotic part of the potential. That is,

$$p_d(t) = \langle\Psi(t)|\Theta(\tilde{r}-\tilde{r}_d)|\Psi(t)\rangle. \tag{E1}$$

The $\tilde{r}_d$ was chosen as 14.0, corresponding to an N–H bond length of 2.4 Å.

The probability of dissociation $p_d(t)$ was computed by integrating over time the flux $F(t;\tilde{r}_d)$ passing through a dividing surface placed at $\tilde{r}_d$, calculated as the expectation value of the flux operator $\hat{F}(\tilde{r}_d)$,

$$\hat{F}(\tilde{r}_d) = i\left[\hat{T}_n, \Theta(\tilde{r}-\tilde{r}_d)\right], \tag{E2}$$

where atomic units are used. State-resolved probabilities of dissociation, $p_d^{(\sigma)}(t)$, were calculated from the integral over time of the expectation value of the projected flux operator $\hat{F}^{(\sigma)}(\tilde{r}_d)$, defined as

$$\hat{P}_\sigma\hat{F}(\tilde{r}_d)\hat{P}_\sigma, \tag{E3}$$

where $\hat{P}_\sigma = |\Phi_\sigma\rangle\langle\Phi_\sigma|$ is the projector onto the σth electronic state.

APPENDIX F: ESTIMATION OF TIME SCALES FOR MONOMERIZATION

To derive estimates for the time scale for the splitting of pyrrole dimer into monomers following photoexcitation, one-dimensional numerically exact wavepacket propagations were performed with initial states corresponding to vertical excitation to the $\tilde{A}(\pi 3s/\sigma^*)$ and $\tilde{B}(\pi 3s/3p/\sigma^*)$ states. In these calculations, the wavepacket was represented in terms of a time-independent exponential DVR basis $\{\chi_i(\tilde{R})\}$,[43]

$$\Psi(\tilde{R},t) = \sum_{\sigma=1}^{n_s}\sum_{i=1}^{N} C_i^{(\sigma)}(t)|\Phi_\sigma\rangle\chi_i(\tilde{R}). \tag{F1}$$

For both excitation to the $\tilde{A}(\pi 3s/\sigma^*)$ and $\tilde{B}(\pi 3s/3p/\sigma^*)$ states, 401 DVR functions were used, with an associated grid ranging from $\tilde{R} = -15$ to $\tilde{R} = +25$. The $\tilde{B}(\pi 3s/3p/\sigma^*)$ state potential along $\tilde{R}$ is unbound, and so the model Hamiltonian was augmented with a CAP. The CAP parameters used [see Eq. (D5)] were $\tilde{R}_c = 15$, $\eta = 0.0003$, and $m = 3$.

REFERENCES

[1] M. N. R. Ashfold, G. A. King, D. Murdock, M. G. D. Nix, T. A. A. Oliver, and A. G. Sage, Phys. Chem. Chem. Phys. **12**, 1218 (2010).
[2] A. L. Sobolewski and W. Domcke, Chem. Phys. **259**, 181 (2000).
[3] B. Cronin, M. G. D. Nix, R. H. Qadiri, and M. N. R. Ashfold, Phys. Chem. Chem. Phys. **6**, 5031 (2004).
[4] A. J. van den Brom, M. Kapelios, T. N. Kitsopoulos, N. H. Nahler, B. Cronin, and M. N. R. Ashfold, Phys. Chem. Chem. Phys. **7**, 892 (2005).
[5] B. Cronin, A. L. Devine, M. G. D. Nix, and M. N. R. Ashfold, Phys. Chem. Chem. Phys. **8**, 3440 (2006).
[6] M. N. R. Ashfold, B. Cronin, A. L. Devine, R. N. Dixon, and M. G. D. Nix, Science **312**, 1637 (2006).

Published under license by AIP Publishing

[7]S. P. Neville and G. A. Worth, J. Chem. Phys. **140**, 034317 (2014).
[8]G. Wu, S. P. Neville, O. Schalk, T. Sekikawa, M. N. R. Ashfold, G. A. Worth, and A. Stolow, J. Chem. Phys. **142**, 074302 (2015).
[9]G. Wu, S. P. Neville, O. Schalk, T. Sekikawa, M. N. R. Ashfold, G. A. Worth, and A. Stolow, J. Chem. Phys. **144**, 014309 (2016).
[10]G. M. Roberts, C. A. Williams, J. D. Young, S. Ulrich, M. J. Paterson, and V. G. Stavros, J. Am. Chem. Soc. **134**, 12578 (2012).
[11]R. Spesyvtsev, O. M. Kirkby, and H. H. Fielding, Faraday Discuss. **157**, 165 (2012).
[12]F. Wang, S. P. Neville, R. Wang, and G. A. Worth, J. Chem. Phys. A **117**, 7298 (2013).
[13]A. L. Sobolewski and W. Domcke, Chem. Phys. Lett. **315**, 293 (1999).
[14]A. L. Sobolewski and W. Domcke, J. Phys. Chem. A **105**, 9275 (2001).
[15]A. Iqbal and V. G. Stavros, J. Phys. Chem. A **114**, 68 (2010).
[16]M. N. R. Ashfold, A. L. Devine, R. N. Dixon, G. A. King, M. G. D. Nix, and T. A. A. Oliver, Proc. Natl. Acad. Sci. U. S. A. **105**, 12701 (2008).
[17]H. Yu, N. L. Evans, V. G. Stavros, and S. Ullrich, Phys. Chem. Chem. Phys. **14**, 6266 (2012).
[18]T. S. Venkatesan, S. G. Ramesh, Z. Lan, and W. Domcke, J. Chem. Phys. **136**, 174312 (2012).
[19]D. B. Bucher, B. M. Piles, T. Carell, and W. Zinth, Proc. Natl. Acad. Sci. U. S. A. **111**, 4369 (2014).
[20]Y. Zhang, J. Dood, A. A. Beckstead, X.-B. Li, K. V. Nguyen, C. J. Burrows, R. Improta, and B. Kohler, Proc. Natl. Acad. Sci. U. S. A. **111**, 11612 (2014).
[21]Y. Zhang, X.-B. Li, A. M. Fleming, J. Dood, A. A. Beckstead, A. M. Orendt, C. J. Burrows, and B. Kohler, J. Am. Chem. Soc. **138**, 7395 (2016).
[22]R. Improta and V. Barone, Angew. Chem. **123**, 12222 (2011).
[23]L. Blancafort and A. A. Voityuk, J. Chem. Phys. **140**, 095102 (2014).
[24]R. Improta, F. Santoro, and L. Blancafort, Chem. Rev. **116**, 3540 (2016).
[25]S. P. Neville, O. M. Kirkby, N. Kaltsoyannis, G. A. Worth, and H. H. Fielding, Nat. Commun. **7**, 11357 (2016).
[26]R. Montero, I. Léon, J. A. Fernández, and A. Longarte, J. Phys. Chem. Lett. **7**, 2797 (2016).
[27]P. Slavíček and M. Fárník, Phys. Chem. Chem. Phys. **13**, 12123 (2011).
[28]M. Duchi, M. P. O'Hagan, R. Kumar, S. J. Bennie, M. C. Galan, B. F. E. Curchod, and T. A. A. Oliver, Phys. Chem. Chem. Phys. **21**, 14407 (2019).
[29]H. Köppel, W. Domcke, and L. S. Cederbaum, *Conical Intersections: Electronic Structure, Dynamics and Spectroscopy* (World Scientific Publishing, 2004), Vol. 15, Chap. 7, p. 323.
[30]G. A. Worth and L. S. Cederbaum, Annu. Rev. Phys. Chem. **55**, 127 (2004).
[31]H. D. Meyer, U. Manthe, and L. S. Cederbaum, Chem. Phys. Lett. **165**, 73 (1990).
[32]M. H. Beck, A. Jäckle, G. A. Worth, and H. D. Meyer, Phys. Rep. **324**, 1 (2000).
[33]G. A. Worth, H.-D. Meyer, H. Köppel, L. S. Cederbaum, and I. Burghardt, Int. Rev. Phys. Chem. **27**, 569 (2008).
[34]G. A. Worth, K. Giri, G. Richings, I. Burghardt, M. H. Beck, A. Jäckle, and H. D. Meyer, The quantics package, version 1.1, University of Birmingham, Birmingham, UK, 2015.
[35]S. A. Bäppler, F. Plasser, M. Wormit, and A. Dreuw, Phys. Rev. A **90**, 052521 (2014).
[36]F. Plasser, B. Thomitzni, S. A. Bäppler, J. Wenzel, D. R. Rehn, M. Wormit, and A. Dreuw, J. Comput. Chem. **36**, 1609 (2015).
[37]S. A. Mewes, F. Plasser, A. Krylov, and A. Dreuw, J. Chem. Theory Comput. **14**, 710 (2018).
[38]S. A. Mewes and A. Dreuw, Phys. Chem. Chem. Phys. **21**, 2843 (2019).
[39]I. Lyskov, M. Kleinschmidt, and C. M. Marian, J. Chem. Phys. **144**, 034104 (2016).
[40]N. Elfers, I. Lyskov, J. D. Spiegel, and C. M. Marian, J. Phys. Chem. C **120**, 13901 (2016).
[41]R. L. Martin, J. Chem. Phys. **118**, 4775 (2003).
[42]J. C. Light, I. P. Hamilton, and J. V. Lill, J. Chem. Phys. **82**, 1400 (1985).
[43]D. T. Colbert and W. H. Miller, J. Chem. Phys. **96**, 1982 (1992).
[44]"TURBOMOLE V6.1 2009, a development of University of Karlsruhe and Forschungszentrum Karlsruhe GmbH, 1989–2007, TURBOMOLE GmbH, 2007, available from http://www.turbomole.com.
[45]H. Lischka, R. Shepard, I. Shavitt, R. M. Pitzer, M. Dallos, T. Mller, P. G. Szalay, F. B. Brown, R. Ahlrichs, H. J. Bhm, A. Chang, D. C. Comeau, R. Gdanitz, H. Dachsel, C. Ehrhardt, M. Ernzerhof, P. Hchtl, S. Irle, G. Kedziora, T. Kovar, V. Parasuk, M. J. M. Pepper, P. Scharf, H. Schiffer, M. Schindler, M. Schler, M. Seth, E. A. Stahlberg, J.-G. Zhao, S. Yabushita, Z. Zhang, M. Barbatti, S. Matsika, M. Schuurman, D. R. Yarkony, S. R. Brozell, E. V. Beck, J.-P. Blaudeau, M. Ruckenbauer, B. Sellner, F. Plasser, and J. J. Szymczak, an *ab initio* electronic structure program, release 7.0, Columbus, 2015.

Published under license by AIP Publishing